

# Selection of intracellular calcium patterns in a model with clustered $\text{Ca}^{2+}$ release channels

J. W. Shuai\* and P. Jung

*Department of Physics and Astronomy and Quantitative Biology Institute, Ohio University, Athens, Ohio 45701*

(Received 18 September 2002; published 13 March 2003)

A two-dimensional model is proposed for intracellular  $\text{Ca}^{2+}$  waves, which incorporates both the discrete nature of  $\text{Ca}^{2+}$  release sites in the endoplasmic reticulum membrane and the stochastic dynamics of the clustered inositol 1,4,5-triphosphate ( $\text{IP}_3$ ) receptors. Depending on the  $\text{Ca}^{2+}$  diffusion coefficient and concentration of  $\text{IP}_3$ , various spontaneous  $\text{Ca}^{2+}$  patterns, such as calcium puffs, local waves, abortive waves, global oscillation, and tide waves, can be observed. We further investigate the speed of the global waves as a function of the  $\text{IP}_3$  concentration and the  $\text{Ca}^{2+}$  diffusion coefficient and under what conditions the spatially averaged  $\text{Ca}^{2+}$  response can be described by a simple set of ordinary differential equations.

DOI: 10.1103/PhysRevE.67.031905

PACS number(s): 87.16.Ac, 05.40.-a, 87.15.Aa, 02.50.Fz

## INTRODUCTION

Calcium ions are ubiquitous in cells as intracellular messengers [1].  $\text{Ca}^{2+}$  participates in a wide range of processes.  $\text{Ca}^{2+}$  triggers life at fertilization, and controls the development and differentiation of cells into specialized types. It can mediate the subsequent activity of cells. Different genes can be activated by varying the frequency or amplitude of  $\text{Ca}^{2+}$  signals [2]. However, a very high concentration of  $\text{Ca}^{2+}$  is no more a signal of life, but a signal of death, which is invariably involved in cell death [1].

The release of calcium ions from internal stores, e.g., the endoplasmic reticulum (ER) or sarcoplasmic reticulum (SR), into the cytosol plays a central role for calcium signals in many excitable and nonexcitable cells. Inositol triphosphate receptors ( $\text{IP}_3\text{Rs}$ ) and ryanodine receptors ( $\text{RyRs}$ ) represent the two major types of intracellular calcium release channels on the ER or SR membrane. Binding with inositol triphosphate ( $\text{IP}_3$ ) messenger and  $\text{Ca}^{2+}$ , the  $\text{IP}_3\text{R}$  causes the release of a small amount of  $\text{Ca}^{2+}$ . The  $\text{IP}_3\text{R}$  closes when the local  $\text{Ca}^{2+}$  concentration becomes large due to the binding of  $\text{Ca}^{2+}$  to an inactivation site. In this manner, the opening and closing of the individual channel causes a localized fundamental  $\text{Ca}^{2+}$  release event, i.e., the  $\text{Ca}^{2+}$  blip [3].

Recently, it has been revealed that in many cells the cytoplasm does not act as a continuous, homogeneous excitable medium to generate  $\text{Ca}^{2+}$  release. Instead,  $\text{Ca}^{2+}$  liberation occurs at discrete functional release sites, spaced a few micrometers apart, which generate localized, elementary  $\text{Ca}^{2+}$  signaling events, termed puffs or sparks [4,5]. The puff sites are believed to be formed by clusters of  $\text{IP}_3\text{Rs}$  distributed on the ER membrane. Each cluster is comprised of a few tens of intact  $\text{IP}_3\text{Rs}$  [6,7]. The spontaneous opening of one channel may cause more channels to open in a positive feedback process called calcium-induced calcium release, in turn generating puffs. Puffs can arise spontaneously with broad range of amplitudes and lifetimes and interpuff intervals [8,9].

$\text{Ca}^{2+}$  puffs function as elementary building blocks

through which various  $\text{Ca}^{2+}$  waves can be generated [10]. By coordinating the spatially discrete  $\text{Ca}^{2+}$  release events, a  $\text{Ca}^{2+}$  wave can be generated, which spreads throughout the cell [11,12]. Such intracellular waves can spread into neighboring cells through some coupling dynamics, resulting in intercellular waves [13]. Globally intracellular or intercellular  $\text{Ca}^{2+}$  signals can display spatially and temporally complex patterns. The temporal patterns of  $\text{Ca}^{2+}$  observed in a variety of cells include oscillations or repetitive spikes. Some cells, most notably *Xenopus* oocytes, also exhibit interesting spatial patterns, including propagating waves, target or spiral patterns [11,12].

As a result, the calcium signals show a hierarchical organization from highly localized blips and puffs to global intracellular or intercellular waves. The hierarchical calcium signals can regulate many different cellular processes, locally or globally. For example,  $\text{Ca}^{2+}$  sparks in smooth muscle cells, which arise locally and near the plasma membrane, activate potassium channels, causing the muscle to relax. But when localized release events deeper in the cell are coordinated to create a global  $\text{Ca}^{2+}$  signal, the muscle contracts [1]. The spatially clustered  $\text{IP}_3\text{R}$  organization enables  $\text{Ca}^{2+}$  to activate opposing cellular responses in the same cell but at different levels.

Experimentally, the two easily controlled parameters for cells are  $\text{IP}_3$  concentration and calcium diffusion.  $\text{IP}_3$  concentration can be stimulated and adjusted by the binding of an extracellular agonist such as a hormone or a neurotransmitter to receptors in the surface membrane [8]. A weak  $\text{Ca}^{2+}$  diffusion can be achieved by intracellularly loading with  $\text{Ca}^{2+}$  buffer EGTA. Depending on the  $\text{IP}_3$  concentration and  $\text{Ca}^{2+}$  diffusion, different patterns of  $\text{Ca}^{2+}$  release can be observed. Puffs are easily observed with the loading of EGTA even at large  $\text{IP}_3$  concentration [9,14]. It has been shown that in *Xenopus* oocytes,  $\text{Ca}^{2+}$  puffs can be observed in narrow regions at low  $\text{IP}_3$  concentration in the absence of EGTA [5,8]. At slightly higher concentrations of  $\text{IP}_3$ , abortive calcium waves travel only short distances [5]. At high  $\text{IP}_3$  concentration, a large tide of  $\text{Ca}^{2+}$  release with no repetitive  $\text{Ca}^{2+}$  waves are observed [12]. At intermediate concentrations of  $\text{IP}_3$ , repetitive  $\text{Ca}^{2+}$  waves are obtained.

Numerically, the intracellular  $\text{Ca}^{2+}$  waves are widely

\*Corresponding author. FAX: 740 593 0433. Email address: shuai@helios.phy.ohiou.edu

simulated by approximating the  $\text{Ca}^{2+}$  channels as a deterministic and spatially continuous source term [15–17]. These reaction-diffusion models explain the observed  $\text{Ca}^{2+}$  patterns as nonlinear waves in an excitable, oscillatory, or bistable medium [15,18,19]. To elucidate the transition from localized to traveling patterns, the clustered distributions of the  $\text{Ca}^{2+}$  release have been taken into account [20–23]. With deterministic models of clustered  $\text{Ca}^{2+}$  release, different forms of waves such as pinned waves, saltatory spreading wave, and abortive wave have been observed [18,23]. The simulation shows that the speed of spreading waves is proportional to the diffusion constant of calcium, rather than its square root in continuous medium case.

The observation of localized stochastic  $\text{Ca}^{2+}$  puffs created by the cluster of a few tens of  $\text{IP}_3\text{Rs}$  [8,9], however, suggests that stochastic effects of channel dynamics are relevant for  $\text{Ca}^{2+}$  wave propagation and need to be taken into account in models. Recently, several such models with stochastic and spatially discrete  $\text{IP}_3\text{R}$  sources have been proposed [18,24,25]. Keizer and Smith [18] introduced a spatially one-dimensional, stochastic model with a clustered distribution of  $\text{Ca}^{2+}$  release channels for cardiac myocytes, showing a transition from spark to wave. Another stochastic model based on the stochastic version of the De Young–Keizer model [26] put forward by Falcke *et al.* [24] shows a transition from spark to abortive wave to steady wave in one-spatial dimension. A backfiring state is observed in a two-dimensional version of the model due to stochastic channel dynamics.

In this paper, we present a model for intracellular  $\text{Ca}^{2+}$  dynamics that consists of a two-dimensional array of clustered, stochastic  $\text{Ca}^{2+}$  release channels mimicking the endoplasmic reticulum. With the goal of reducing CPU demand, our model for the local  $\text{Ca}^{2+}$  release is based on the stochastic version [27,28] of the Li-Rinzel model [29]. Our model reproduces in two dimensions the experimentally observed transition from calcium puffs to abortive waves and global oscillatory patterns when the level of  $\text{IP}_3$  and calcium diffusion, i.e.,  $[\text{IP}_3]$  and  $D$ , increases. It further shows that the local and abortive waves can be observed between the regions of puffs and global waves. At high  $[\text{IP}_3]$  levels, we observe the transition to another experimentally observed wave type, i.e., tide waves [12]. For global oscillation, sandwiched between the abortive waves and the tide waves with respect to the concentration of  $\text{IP}_3$ , we confirm the prediction from the one-dimensional model that the average speed of the wave increases linearly with the  $\text{Ca}^{2+}$  diffusion coefficient [18]. In addition we find that the wave speed exhibits a bell-shaped curve as a function of the concentration of  $\text{IP}_3$  vanishing at the interfaces to the local and abortive waves and the tide waves.

## THEORETICAL MODEL

In our model, the intracellular calcium dynamics is described by a reaction-diffusion model with stochastic  $\text{IP}_3\text{R}$  channel sources, discretely distributed on a two-dimensional ER membrane:

$$\frac{d[\text{Ca}^{2+}](x,y)}{dt} = D\nabla^2[\text{Ca}^{2+}](x,y) + f(x,y)(J_{\text{Channel}} - J_{\text{Pump}} + J_{\text{Leak}}), \quad (1)$$

$$\frac{d[\text{Ca}^{2+}]_{\text{ER}}(x,y)}{dt} = D_{\text{ER}}\nabla^2[\text{Ca}^{2+}]_{\text{ER}}(x,y) - \frac{1}{\alpha}f(x,y) \times (J_{\text{Channel}} - J_{\text{Pump}} + J_{\text{Leak}}), \quad (2)$$

where  $[\text{Ca}^{2+}]$  and  $[\text{Ca}^{2+}]_{\text{ER}}$  are the concentrations of  $\text{Ca}^{2+}$  in the cytoplasm and internal stores, respectively. The diffusion constants in the cytoplasm and the ER pool, i.e.,  $D$  and  $D_{\text{ER}}$ , include fast buffering effects and are effective diffusion constants. The factor  $\alpha$  is the ratio of the volume of the ER pool to the cytosolic volume. Our model describes an isolated cell where the total amount of  $\text{Ca}^{2+}$  is conserved; only the exchange of  $\text{Ca}^{2+}$  between the cytoplasm and the ER is taken into account;  $\text{Ca}^{2+}$  flux through the cellular membrane is neglected.

Three calcium fluxes are considered for  $\text{Ca}^{2+}$  release dynamics: (i) the channel flux  $J_{\text{Channel}}$  from the ER to the intracellular space through the  $\text{IP}_3\text{R}$  channels, (ii) the pump flux  $J_{\text{Pump}}$  from the intracellular space into the ER with the ATP (adenosine triphosphate) dependent pump, and (iii) the leakage flux  $J_{\text{Leak}}$  from the ER to the intracellular space. The function  $f(x,y)$  represents the inhomogeneous distribution of the  $\text{Ca}^{2+}$  release sites. Typically, the clustered  $\text{IP}_3\text{R}$  channels are spatially distributed within a few hundreds of nanometers [5,6,8] and the nearby  $\text{IP}_3\text{R}$  clusters are several micrometers [9,22] apart on average. A homogeneous  $\text{Ca}^{2+}$  ATPase pump is assumed in calcium release models [18,25]. The experiment with astrocyte cells indicated that the discrete release regions of  $\text{Ca}^{2+}$  are separated by regions that may be passively diffusing [20,30]. Similar to the models in Refs. [20,21], we consider the membrane as a mosaic of active and passive patches. In our model, both the  $\text{IP}_3\text{R}$  channels and the  $\text{Ca}^{2+}$  pumps are assumed to be distributed in the active regions. In detail, a regular array of active regions separated by regions of passive diffusion is considered, i.e.,

$$f(x,y) = \sum_i \sum_j \left[ \Theta\left(x - iL - \frac{l}{2}\right) - \Theta\left(x - iL + \frac{l}{2}\right) \right] \times \left[ \Theta\left(y - jL - \frac{l}{2}\right) - \Theta\left(y - jL + \frac{l}{2}\right) \right], \quad (3)$$

with the Heaviside function  $\Theta(x) = 0$  for  $x \leq 0$ , otherwise 1. Each active region is a square with a side length of  $l$  and two nearby active regions have a distance of  $L$ . Consistent with the experimental data, we choose  $l = 0.15 \mu\text{m}$  and  $L = 2.0 \mu\text{m}$ .

Various models have been proposed for the calcium release dynamics [6,15,26]. Differences among these models arise mainly in the different kinetic schemes of binding  $\text{IP}_3$  and  $\text{Ca}^{2+}$  to activating and inhibiting sites of the  $\text{IP}_3\text{R}$ . The key issue is how the  $\text{IP}_3$  and  $\text{Ca}^{2+}$  binding and unbinding rates depend on the state of the receptor and the concentration of  $\text{IP}_3$  and  $\text{Ca}^{2+}$ . A theoretical model for agonist-

induced  $[Ca^{2+}]$  oscillations based on microscopic kinetics of  $IP_3$  and  $[Ca^{2+}]$  gating of the  $IP_3R$  was proposed by De Young and Keizer [26]. The model assumes that three equivalent and independent subunits are involved in the conduction of an  $IP_3R$ . Each subunit has one  $IP_3$  binding site ( $m$  gate) and two  $Ca^{2+}$  binding sites, one for activation ( $n$  gate), the other for inhibition ( $h$  gate). A simplified version of the model was proposed by Li and Rinzel [29], in which the  $m$  and  $n$  gates are substituted by their steady state values,  $m_\infty$  and  $n_\infty$ . Due to its slow time scale, the  $h$  gate is considered as a variable in the deterministic Li-Rinzel model.

The small number of  $IP_3R$ s in a single cluster generates stochastic conductance. Following the deterministic Li-Rinzel model, we only consider the stochastic opening and closing processes of gate  $h$ . Only if all three inactivation sites of the three subunits, i.e.,  $h$  gates, are nonoccupied by  $Ca^{2+}$ , the channel is  $h$  disinactivated or termed  $h$  open in the paper. The stochastic version of the Li-Rinzel model is then described by Ref. [27,28]:

$$J_{\text{Channel}} = \alpha v_1 m_\infty^3 n_\infty^3 \frac{N_{h\text{-open}}}{N} ([Ca^{2+}]_{ER} - [Ca^{2+}]), \quad (4)$$

$$J_{\text{Pump}} = \frac{v_3 [Ca^{2+}]^2}{k_3^2 + [Ca^{2+}]^2}, \quad (5)$$

$$J_{\text{Leak}} = \alpha v_2 ([Ca^{2+}]_{ER} - [Ca^{2+}]), \quad (6)$$

with

$$m_\infty = \frac{[IP_3]}{[IP_3] + d_1},$$

$$n_\infty = \frac{[Ca^{2+}]}{[Ca^{2+}] + d_5}, \quad (7)$$

where  $N$  and  $N_{h\text{-open}}$  in Eq. (4) indicate the total number of  $IP_3R$  channels and the number of  $h$ -open channels in a cluster, respectively.

The deterministic Li-Rinzel model suggests that the closing (C) and opening (O) of the three  $h$  sites can be described by independent two-state Markov processes with opening and closing rates  $\alpha_h$  and  $\beta_h$ , respectively. Thus, we use the stochastic scheme for all three  $h$  gates,



with

$$\alpha_h = a_2 d_2 \frac{[IP_3] + d_1}{[IP_3] + d_3},$$

$$\beta_h = a_2 [Ca^{2+}]. \quad (9)$$

The stochastic dynamics of Eq. (8) for each single gate is simulated by a two-state Markov process.

TABLE I. Parameters of the model.

Parameter	Value
$[IP_3]$	Varies ( $\mu M$ )
$D$	Varies ( $\mu m^2/sec$ )
$D_{ER}$	$0.45 \mu m^2/sec$
$l$	$0.15 \mu m$
$L$	$2.0 \mu m$
$N$	20
$S$	$60 \mu m \times 60 \mu m$
$\alpha$	0.185
$v_1$	$1166.7 sec^{-1}$
$v_2$	$3.333 sec^{-1}$
$v_3$	$166.7 \mu M/sec$
$k_3$	$0.1 \mu M$
$d_1$	$0.13 \mu M$
$d_2$	$1.049 \mu M$
$d_3$	$0.9434 \mu M$
$d_5$	$0.08234 \mu M$
$a_2$	$0.4 \mu M^{-1} sec^{-1}$
$c_0$	$2.0 \mu M$

As a result, a stochastic model for intracellular  $Ca^{2+}$  waves is designed, which takes into account the clustered distribution of  $IP_3R$ s and their stochastic conductance. The typical parameters used are listed in Table I. In the numerical simulation, the two-dimensional ER membrane is discrete and represented by a two-dimensional (2D) lattice with grid distance  $\Delta x$ . In order to avoid grid sizes small in comparison to the active sites, the active sites are placed on the lattice as *point sources* regardless of their actual physical size. To take into account the actual physical size of the cluster (the strength of the source), the term describing  $Ca^{2+}$  flux density through the  $IP_3R$ s must be rescaled with  $l/\Delta x$ . This procedure allows us to use grid sizes larger than the actual size of the active sites, i.e.,  $\Delta x \geq l$ . The finite-difference representation of Eq. (1) used in our numerical simulation is given by

$$C_{i,j}^{n+1} = C_{i,j}^n + \frac{D\Delta t}{\Delta^2 x} (C_{i+1,j}^n + C_{i-1,j}^n + C_{i,j+1}^n + C_{i,j-1}^n - 4C_{i,j}^n)$$

$$+ \left(\frac{l}{\Delta x}\right)^2 J_{i,j}^n \Delta t \sum_{i',j'} \delta_{i,i'k} \delta_{j,j'k}, \quad (10)$$

where  $C_{i,j}$  is the calcium concentration at location  $(i,j)$ ,  $n$  indicates the discrete time  $n\Delta t$ , and  $J_{i,j}^n$  indicates the sum of three calcium fluxes at site  $(i,j)$  at time  $n\Delta t$ . The locations of active sites are represented by the Kronecker symbols  $\delta_{n,m}$  with  $k=L/\Delta x$ . In our simulation, the grid distance was chosen  $\Delta x = 0.5 \mu m$ , resulting in  $k=4$  and rescale number  $l/\Delta x = 0.3$ . We have tested the accuracy of the results by selective runs at smaller  $\Delta x$ .

The deterministic 2D model with clustered but nonstochastic active sites is obtained with the following channel flux, rather than Eq. (4):

$$J_{\text{Channel}} = c_1 v_1 m_\infty^3 n_\infty^3 h^3 ([\text{Ca}^{2+}] - [\text{Ca}^{2+}]_{ER}), \quad (11)$$

$$\frac{dh}{dt} = \alpha_h(1-h) - \beta_h h. \quad (12)$$

## RESULTS

### Parameter selection

Electron microscopy shows that the distance between two IP<sub>3</sub>Rs is about 12 nm in the dendrites of Purkinje neurons of bovine cerebellum [31]. Electron micrograph of rabbit skeletal muscle shows that the interchannel distance of RyRs is about 31.5 nm [7]. These data suggest that IP<sub>3</sub>R, unlike RyR, may have a compact structure. In the model, we assume that there are  $N=20$  IP<sub>3</sub>R channels in each active site with a size of  $l$ , which is as predicted in Refs. [6,28]. The concentration of IP<sub>3</sub> is assumed constant, since its diffusion coefficient is quite large in comparison to that of Ca<sup>2+</sup>. Similar to that by Roth *et al.* [20], a small diffusion coefficient is used for Ca<sup>2+</sup> in the ER. We start with the initial condition of  $\text{Ca}^{2+}(x,y) + \alpha \text{Ca}_{ER}^{2+}(x,y) = c_0$  [26,29] and apply no-flux boundary condition conserving the total amount of Ca<sup>2+</sup>. The active sites are not placed on the boundaries.

Measured diffusion constants of Ca<sup>2+</sup> ions in cytosolic extracts of *Xenopus* oocytes assume values between 10 μm<sup>2</sup>/sec (buffered) and 220 μm<sup>2</sup>/sec (free ions) [32]. Typically, the effective diffusion coefficient  $D$  is about 20–30 μm<sup>2</sup>/sec [15,21]. The parameters listed in Table I are selected such that the spreading velocity of the intracellular calcium wave is about 25 μm/sec and the oscillating frequency is 0.09 Hz at  $D=20$  μm<sup>2</sup>/sec and  $[\text{IP}_3]=0.5$  μM, consistent with those observed in *Xenopus* [11,12].

Furthermore, the three flux parameters  $v_1$ ,  $v_2$ , and  $v_3$  are determined such that the spatially averaged Ca<sup>2+</sup> concentration obtained from the deterministic 2D model [i.e., Eqs. (1)–(3), (5)–(7), and (9)–(12)] as a function of time exhibits a bifurcation diagram (in  $[\text{IP}_3]$ - $[\text{Ca}^{2+}]$  space) that approximates closely the bifurcation diagram of the original Li-Rinzel model (designed for whole cell Ca<sup>2+</sup> response). To match the oscillation frequency of the spatially averaged Ca<sup>2+</sup> concentrations to those of the original Li-Rinzel model, the factor  $a_2$  occurring in the opening and closing rates of the  $h$  gate had to be adjusted. The other parameters for the channel dynamics are the same as those for the Li-Rinzel model [29].

As a result, we obtain the parameters listed in Table I. With this choice of parameters, the microscopic model for the Ca<sup>2+</sup> release from single clusters—for the given distribution of clusters—is consistent with the original Li-Rinzel model for the cell-averaged response [32].

The spatiotemporal bifurcation diagram of the cell-averaged Ca<sup>2+</sup> concentration

$$\langle \text{Ca}^{2+}(t) \rangle = \frac{1}{S} \int_S [\text{Ca}^{2+}](x,y,t) dx dy \quad (13)$$

(maximum and minimum in the oscillatory regime) of deterministic 2D model is compared to the bifurcation diagram of

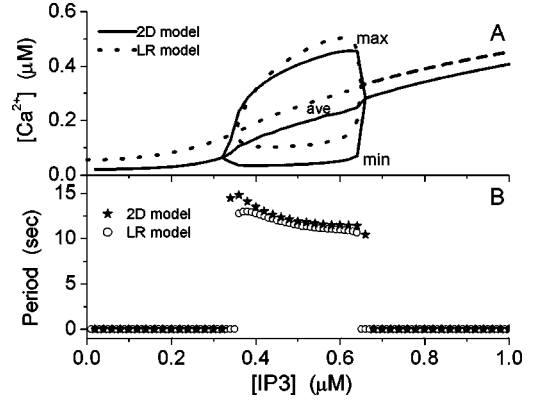


FIG. 1. (A) The mean value and the bifurcation diagram of the cell-averaged calcium signals of the two-dimensional deterministic model as a function of  $[\text{IP}_3]$  at  $D=20$  μm<sup>2</sup>/sec (solid line) are compared with the mean value and the bifurcation diagram of the original Li-Rinzel model (dashed line). (B) The oscillation period of the cell-averaged calcium signals of the two-dimensional deterministic model (stars) is compared with the oscillation period of the original Li-Rinzel model (circles).

the original Li-Rinzel model in Fig. 1(A). The comparison of the oscillation periods in the range of (0.34 μM, 0.64 μM) is shown in Fig. 1(B).

### Selection of spontaneous Ca<sup>2+</sup> patterns

Due to the stochasticity of IP<sub>3</sub>Rs, one can observe various spontaneous Ca<sup>2+</sup> patterns for various concentrations of IP<sub>3</sub> and diffusion coefficients  $D$ . First, we study how  $[\text{IP}_3]$  and  $D$  affect the averaged Ca<sup>2+</sup> concentrations and the bifurcation diagram. The spatially and temporally averaged intracellular Ca<sup>2+</sup> concentration

$$\overline{\langle \text{Ca}^{2+}(t) \rangle} = \frac{1}{T} \lim_{T \rightarrow \infty} \int_0^T \langle \text{Ca}^{2+}(t) \rangle dt \quad (14)$$

as a function of the concentration of IP<sub>3</sub> is shown in Fig. 2(a). One can see that  $\overline{\langle \text{Ca}^{2+}(t) \rangle}$  is increasing with increasing  $[\text{IP}_3]$ , but is rather insensitive to  $D$ . The bifurcation diagram for the spatially averaged Ca<sup>2+</sup> concentration, however, strongly depends on  $D$  [see Fig. 2(b)]. For large  $D$ , the coupling between the active sites is strong and as a consequence, nearby active sites act more synchronously. For small  $D$ , the active sites are rather independent and the stochastic Ca<sup>2+</sup> release of the individual active site averages out. In between, groups of active sites synchronize and the spatial averaging yields a weak oscillatory signal. The amplitude of the oscillations increases with increasing synchrony for large  $D$ , approaching the deterministic bifurcation diagram [Fig. 1(A)].

Figure 3 shows series of snapshots of some typical intracellular calcium patterns obtained with our two-dimensional stochastic model for various  $[\text{IP}_3]$  and  $D$ , including puffs, local waves, abortive waves, global oscillatory patterns, and tide waves. A corresponding (sketchy) phase diagram that visualizes the pattern selection process is shown in Fig. 4.

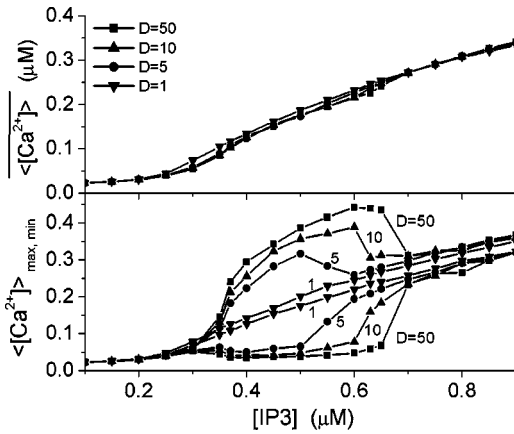


FIG. 2. Cell-averaged calcium signals  $\langle Ca^{2+}(t) \rangle$  of the stochastic two-dimensional model as a function of  $[IP_3]$  for  $D=50, 10, 5,$  and  $1 \mu m^2/sec$ . The top panel shows the time-averaged signal  $\langle Ca^{2+}(t) \rangle$ . The bottom panel shows the maximum value and minimum values of the calcium signal  $\langle Ca^{2+}(t) \rangle$ .

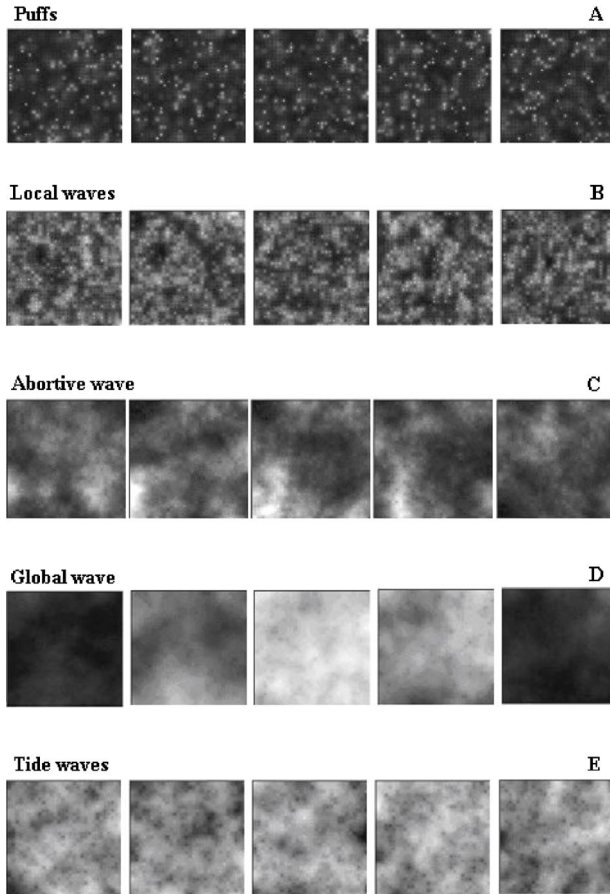


FIG. 3. Simulated  $Ca^{2+}$  waves for various  $D$  and  $[IP_3]$ . (A) Calcium puffs for  $D=1 \mu m^2/sec$  and  $[IP_3]=0.3 \mu M$ ; (B) Local waves for  $D=2 \mu m^2/sec$  and  $[IP_3]=0.5 \mu M$ ; (C) Abortive wave for  $D=10 \mu m^2/sec$  and  $[IP_3]=0.35 \mu M$ ; (D) Oscillating wave for  $D=20 \mu m^2/sec$  and  $[IP_3]=0.5 \mu M$ ; (E) Tide waves for  $D=10 \mu m^2/sec$  and  $[IP_3]=0.8 \mu M$ . The time interval for two continued snapshots is 2 sec for all waves. Bright gray levels indicate high  $Ca^{2+}$  concentration.

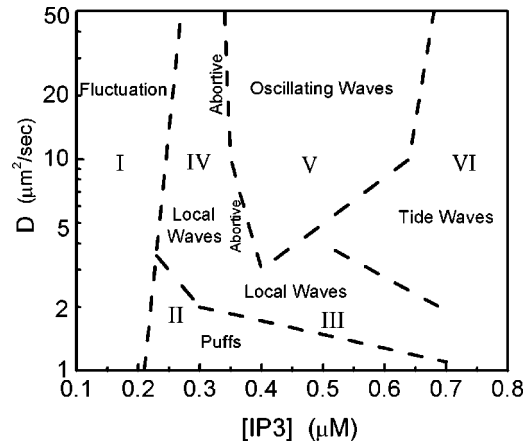


FIG. 4. Phase diagram of various  $Ca^{2+}$  patterns in the  $[IP_3]$ - $D$  plane.

For small  $[IP_3]$ , the release of calcium is so small that calcium signals can hardly be observed (i.e., region I in Fig. 4).

Different patterns also show different spatial coherence of active sites. The spatial coherence can be characterized by the correlation function

$$\xi(d) = \frac{\langle (x_0 - \langle x_0 \rangle)(x_d - \langle x_d \rangle) \rangle}{[\langle (x_0 - \langle x_0 \rangle)^2 \rangle]^{1/2} [\langle (x_d - \langle x_d \rangle)^2 \rangle]^{1/2}}, \quad (15)$$

where  $\langle \cdot \rangle$  denotes the time average,  $x_0(t)$  the  $Ca^{2+}$  concentration of the active site at the center of the 2D stochastic model, and  $x_d(t)$  the  $Ca^{2+}$  signal of an active site at a distance of  $d$  from the center. Figure 5 shows the correlation functions for the five typical waves given in Fig. 3.

In the following, we discuss in detail the properties of these waves. It is important to note that the transitions between these typical patterns, i.e., puffs, local waves, abortive waves, global oscillation and tide waves, are gradual. The distinction lines shown in Fig. 4 should be interpreted accordingly.

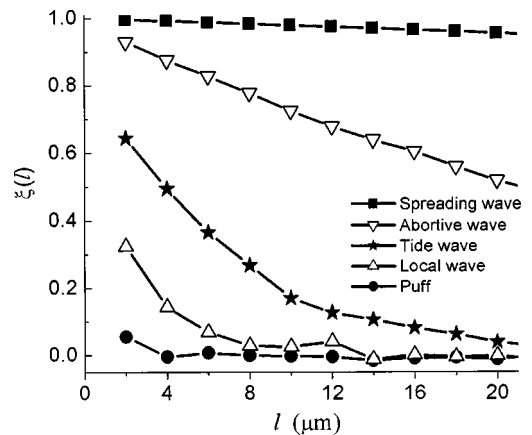


FIG. 5. Comparison of the spatial correlation function  $\xi(d)$  of calcium release for different types of calcium patterns that are discussed in Fig. 3. The distance  $d$  is changed discretely from  $2 \mu m$  to  $20 \mu m$ .

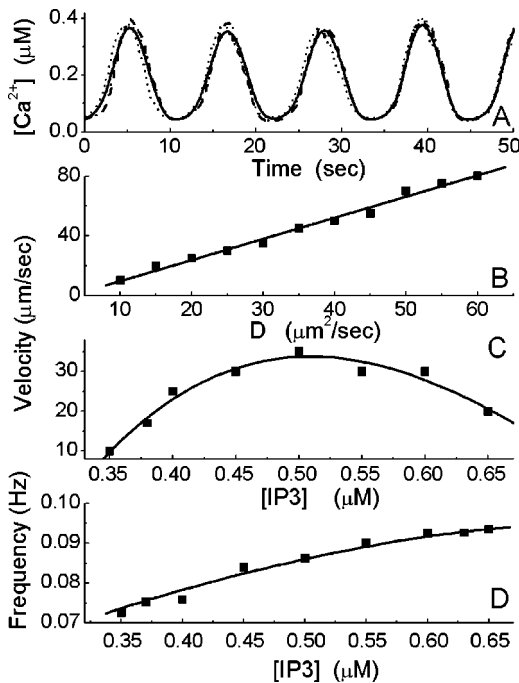


FIG. 6. Properties of oscillating waves. (A) depicts four  $Ca^{2+}$  signals as a function of time at  $D=20 \mu m^2/sec$  and  $[IP_3]=0.5 \mu M$ . The solid line indicates the cell-averaged  $Ca^{2+}$  signal. The dotted line and long dashed line indicate  $Ca^{2+}$  release signals of two nearby active sites in the center area of the cell model. The short dashed line represents  $Ca^{2+}$  release signals of an active site at a distance of  $15 \mu m$  from the central site. The averaged velocity of spontaneous oscillating wave is shown in (B) for  $[IP_3]=0.5 \mu M$  as a function of  $D$  and as a function of  $[IP_3]$  in (C) at  $D=30 \mu m^2/sec$ . A linear functional fit with slope of 1.4 is obtained for the averaged wave speed vs  $D$  in (B). The mean oscillating frequency of the cell-averaged  $Ca^{2+}$  signals  $\langle Ca^{2+}(t) \rangle$  is shown in (D) as a function of  $[IP_3]$  at  $D=30 \mu m^2/sec$ .

### Global oscillation

Oscillatory  $Ca^{2+}$  waves can be observed in *Xenopus* oocytes [11,12]. In our model, spontaneous oscillatory waves occur typically at large  $D$  ( $>5 \mu m^2/sec$ ) and  $0.34 \mu M < [IP_3] < 0.66 \mu M$  (i.e., region V in Fig. 4). In this  $[IP_3]$  regime, the deterministic 2D model predicts oscillatory waves. The stochasticity of the release dynamics (at, e.g.,  $N=20$ ) causes wave initiation throughout the system, which is spatially strongly correlated due to the large diffusion coefficient. This leads to the onset of almost global oscillations [see Fig. 3(D)]. It is important to note that this does not preclude propagating wave front to occur transiently. In the 2D deterministic limit, global oscillation and spreading waves can both occur. The  $IP_3$ R's stochasticity may initiate some local waves. The wave fronts of these local waves spread out and merge into a global wave.

As an example, snapshots of a global oscillatory pattern are shown in Fig. 3(D) for  $D=20 \mu m^2/sec$  and  $[IP_3]=0.5 \mu M$ . The cell-averaged calcium signal and signals at three different active sites (two nearby sites at the center of cell model, the other site having a distance of  $15 \mu m$  from the center) are compared in Fig. 6(A). One can see that the

signals are well synchronized and exhibit little stochasticity (compare also in Fig. 5, where we show the correlation function).

Two important parameters for these spontaneously global patterns are spreading velocity and oscillating frequency. The instantaneous wave velocity is calculated from the shift of the isoconcentration line of  $Ca^{2+}$  in a small time interval. Due to the stochastic  $IP_3$ R dynamics, the instantaneous velocities are varying in time and from site to site. The spreading velocity is defined as the average of the instantaneous velocities. The average velocity of the global wave as a function of  $D$  is shown in Fig. 6(B) for  $[IP_3]=0.5 \mu M$ . The average velocity increases linearly with increasing  $D$ . The increasing rate is 1.4 in this example. The average velocity of the wave versus  $[IP_3]$  is shown in Fig. 6(C) for  $D=30 \mu m^2/sec$ . At the interfaces to the *abortive waves* (at about  $[IP_3]=0.34 \mu M$ ) and *tide waves* (at about  $[IP_3]=0.66 \mu M$ ) the speed of the global wave vanishes. In between it exhibits a maximum.

The oscillating frequency is the average frequency of the cell-averaged signal  $\langle Ca^{2+}(t) \rangle$ . It is shown that the average frequency increases with increasing  $[IP_3]$  [see Fig. 6(D)], while it is insensitive to the diffusion constant  $D$ . For example, the average frequency decreases only from 0.094 Hz to 0.089 Hz with  $D$  increasing from 10 to  $60 \mu m^2/sec$  at  $[IP_3]=0.5 \mu M$ .

### Calcium puffs

Other important types of calcium patterns observed experimentally are calcium puffs or sparks [4,5,8,14]. Our model suggests that the calcium puffs can be observed at low  $D$ . When  $[IP_3]$  is increased beyond  $\approx 0.2 \mu M$ , significant  $Ca^{2+}$  release can be obtained from the active sites. In region II (Fig. 4), the weak diffusive coupling between active sites results in almost independent activity of each active site, i.e., puffs. Because of the stochastic opening dynamics for clustered  $IP_3$ R's, puffs can be also observed in the  $[IP_3]$  region where the deterministic Li-Rinzel model predicts fixed points. Stochastic dynamics causes a broad distribution of puff amplitudes, lifetimes, and interpuff intervals [8,9,28].

A sequence of snapshots is shown in Fig. 3(A) for  $D=1 \mu m^2/sec$  and  $[IP_3]=0.3 \mu M$ . Figure 5 (solid circle) shows that nearby clusters are almost uncorrelated. This weak correlation can also be confirmed by direct observation of  $Ca^{2+}$  signals in Fig. 7(A) where we compare the  $Ca^{2+}$  traces taken at two nearby active sites in the center of our cell model. In Fig. 7(B), we show the  $Ca^{2+}$  concentration in the passive region between the two clusters recorded from Fig. 7(A), and the cell-averaged  $Ca^{2+}$  concentration  $\langle Ca^{2+}(t) \rangle$ . Each time a synchronized  $Ca^{2+}$  release event occurs, the concentration of  $Ca^{2+}$  at the passive site in between the two active sites exhibits a maximum. The small  $Ca^{2+}$  signals in the passive region indicate that the coupling is weak, although a few synchronized releases can be observed in Fig. 7(A). Puffs involving coupled calcium release at adjacent sites were also observed in *Xenopus* oocytes [33].

### Local, abortive, and tide waves

Local waves occur when the diffusion coefficient is large enough so that the diffusion of  $Ca^{2+}$  correlates  $Ca^{2+}$  releases

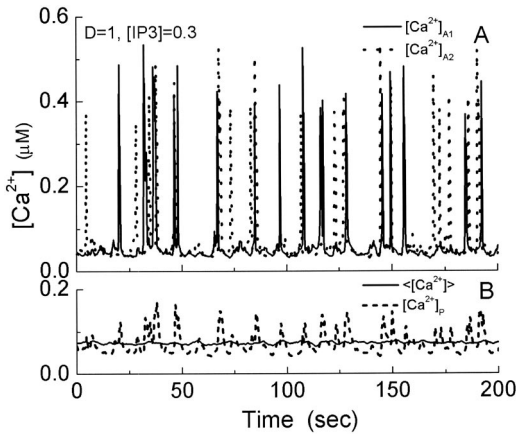


FIG. 7. Trajectories of  $\text{Ca}^{2+}$  puff system at  $D=1 \mu\text{m}^2/\text{sec}$  and  $[\text{IP}_3]=0.3 \mu\text{M}$ . Two calcium traces  $[\text{Ca}^{2+}]_{A1}$  and  $[\text{Ca}^{2+}]_{A2}$  obtained from two nearby active sites ( $A1$  and  $A2$ ) in the center of the cell model for  $D=1 \mu\text{m}^2/\text{sec}$  and  $[\text{IP}_3]=0.3 \mu\text{M}$  are compared in (A). The signal  $[\text{Ca}^{2+}]_P$  obtained from a passive site in between the two active sites ( $A1$  and  $A2$ ) is shown in (B) by a dashed line. The cell-averaged signal  $\langle \text{Ca}^{2+}(t) \rangle$  is shown in (B) by a solid line.

within a small group of active sites [Fig. 3(B)]. Thus local waves can be distinguished from puffs by longer-range correlations (Fig. 5). Local waves occur in regions III (with small  $D$  and deterministically oscillating  $[\text{IP}_3]$ ) and IV (with large  $D$  and deterministically subthreshold  $[\text{IP}_3]$ ) in Fig. 4. The amplitudes of the local waves in region III are typically larger than those in region IV, but the lifetimes in region III are shorter than those in region IV. Dense and small-size local waves are observed in region III [Fig. 3(B)], but rare and large-size local waves are found in region IV. Local waves are randomly initiated and can travel only for a few micrometers before aborting spontaneously. Nearby local waves may collide with each other and merge to a new local wave before abortion. Increasing  $[\text{IP}_3]$  or  $D$  increases the size and the lifetime of local waves. Thus, when approaching the global wave regime by increasing  $[\text{IP}_3]$ , the sizes of the local waves and the spatial correlation increase. This increase in spatial correlation causes a decrease in the spontaneous generation rate of local waves and thus collisions occur less frequent.

At the boundary to the global pattern regime (region V in Fig. 4), one can observe large local waves that abort propagation, termed abortive wave by Callamaras *et al.* [33] and observed in *Xenopus* oocytes. Abortive waves are large local waves close to or at propagation threshold that can become large, but are yet nonpropagating before they disappear spontaneously. The cell-averaged signal  $\langle \text{Ca}^{2+}(t) \rangle$  shows irregular oscillations due to the repetitive production of abortive waves. Figure 3(C) shows an example of an abortive wave. The size and location of abortive waves are varying with time. The spatial correlations of abortive waves are of longer range than for the local waves (Fig. 5).

Yet another type of pattern can be observed in regime VI, termed *tide wave* by Lechleiter *et al.* [12] and observed in *Xenopus* oocytes. Figure 3(E) gives an example of a tide wave at a large concentration of  $\text{IP}_3$  where the deterministic

dynamics is nonoscillatory. A large tide of  $\text{Ca}^{2+}$  release is observed for large  $\text{IP}_3$  concentration where the deterministic 2D model predicts a fixed point. At large  $[\text{IP}_3]$ , many channels are in the open state and the calcium concentration is typically high, compared to the local waves. The stochastic closing of groups of  $\text{IP}_3\text{Rs}$  creates islands of lower  $\text{Ca}^{2+}$  concentrations. These tide waves can be understood as the “photonegative” of the local waves where islands of large  $\text{Ca}^{2+}$  concentration in a sea of low  $\text{Ca}^{2+}$  concentration are replaced by islands of low  $\text{Ca}^{2+}$  concentration in a sea of large  $\text{Ca}^{2+}$  concentration. The spatial correlation of tide wave decays similar to that of the local wave (Fig. 5).

## SUMMARY AND DISCUSSION

We have put forward a 2D model for  $\text{Ca}^{2+}$  release from the ER through discrete active sites. Each active site has been modeled by a stochastic version of the oscillating Li-Rinzel model. The active sites are coupled by diffusion of  $\text{Ca}^{2+}$  through the ER and the intracellular space. Depending on the diffusion coefficient and the  $\text{IP}_3$  concentration, a wealth of patterns can be observed. In this paper, in order to remain consistent with previous literature, we have used terminology introduced in the experimental literature. The difference between wave types are often only of quantitative nature.

Experiments show that the velocity of global  $\text{Ca}^{2+}$  waves increases with increasing  $[\text{IP}_3]$  [20]. Some theoretical models also reproduce such a relationship [20,21]. Our model predicts an increase of the wave speed with increasing  $[\text{IP}_3]$ , a maximum speed, and a subsequent decrease with further increasing concentration of  $[\text{IP}_3]$ . With excitable  $\text{IP}_3\text{R}$  release dynamics in some 1D models, it has been shown that the velocity of saltatorially spreading waves is linearly related to the diffusion coefficient  $D$  in the case of discrete  $\text{IP}_3\text{Rs}$  [18,22,23]. Here we show that such a relationship is still true for the oscillatory waves.

In our model, calcium puffs are typically obtained for small coupling  $D$ . This observation is consistent with the experimental protocol of intracellularly loading with  $\text{Ca}^{2+}$  buffer EGTA [9,14] in order to observe  $\text{Ca}^{2+}$  puffs. However, experiments also show that the puffs can be observed at a low, but narrow range of  $[\text{IP}_3]$  even without loading EGTA for *Xenopus* [5,8]. For our model, with a biological  $D$  (about  $20 \mu\text{m}^2/\text{sec}$ ), one typically finds local waves for small  $[\text{IP}_3]$  (i.e., region IV in Fig. 4). A possible explanation for such a behavior is that the  $\text{IP}_3\text{Rs}$  may have excitable rather than oscillatory release dynamics which is not considered in the paper.

There are two important time scales for calcium signals [23]. One is the  $\text{Ca}^{2+}$  releasing time scale  $\tau_r$  from the  $\text{IP}_3\text{R}$  and the other one is the  $\text{Ca}^{2+}$  diffusion time scale

$$\tau_d = L^2/D,$$

where  $L$  is the distance between two nearby active sites. Puffs should be observed when

$$\tau_r/\tau_d < 1, \quad (16)$$

which means that the releasing event is much faster than the  $\text{Ca}^{2+}$  diffusion between two active sites. In the model, calcium release dynamics is described by the stochastic oscillatory Li-Rinzel model. The releasing time scale of  $\tau_r \approx 1$  sec can be obtained from the puff width distribution (not shown) with the small diffusion coefficient  $D = 0.01 \mu\text{m}^2/\text{sec}$ . The nearby activation sites have a distance of  $L = 2 \mu\text{m}$ , resulting in the condition for puffs  $D < L^2/\tau_r = 4 \mu\text{m}^2/\text{sec}$  consistent with Fig. 4. However, for an excitable model, the release time can be quite fast (e.g., 0.2 sec) so that Eq. (16) may be fulfilled at biological  $D$ .

In *Xenopus* oocytes, one can observe saltatory waves [33]. The condition for a saltatory wave is that [23]

$$\tau_r / \tau_d \ll 1. \quad (17)$$

Spreading waves can be obtained in our model only at  $D > 3 \mu\text{m}^2/\text{sec}$  (Fig. 4). Spreading waves are thus consistent

with  $\tau_r / \tau_d \gg 0.75$ . The conditions for saltatory propagation can therefore not be fulfilled with our oscillatory model, similar as with the stochastic, oscillatory model by Falcke *et al.* [24].

Different pump distributions have been observed in cells or assumed in the models [18,20,21,25,30]. In our model, the ER membrane is considered as a mosaic of active and passive pieces, and the  $\text{Ca}^{2+}$  pumps and  $\text{IP}_3\text{Rs}$  are both placed inside the active regions only, similar to the models in Refs. [20,21]. Because the release channels and also the pumps are highly coupled within the entire cell at physiologically realistic values of  $D$  (see Fig. 5), different pump distributions result in similar patterns.

#### ACKNOWLEDGMENT

This material was based upon work supported by the National Science Foundation under Grant No. IBN-0078055.

- 
- [1] M.J. Berridge, M.D. Bootman, and P. Lipp, *Nature (London)* **395**, 645 (1998).  
 [2] R.E. Dolmetsch, K. Xu, and R.S. Lewis, *Nature (London)* **392**, 933 (1998).  
 [3] M. Bootman, E. Niggli, M. Berridge, and P. Lipp, *J. Physiol. (London)* **499**, 307 (1997).  
 [4] H. Cheng, W.J. Lederer, and M.B. Cannel, *Science* **262**, 740 (1993).  
 [5] Y. Yao, J. Choi, and I. Parker, *J. Physiol. (London)* **482**, 533 (1995).  
 [6] S. Swillens, G. Dupont, L. Combettes, and P. Champeil, *Proc. Natl. Acad. Sci. U.S.A.* **96**, 13 750 (1999).  
 [7] C.C. Yin and F.A. Lai, *Nat. Cell Biol.* **2**, 669 (2000).  
 [8] X. Sun, N. Callamaras, J.S. Marchant, and I. Parker, *J. Physiol. (London)* **509**, 67 (1998).  
 [9] N. Callamaras and I. Parker, *EMBO J.* **19**, 3608 (2000).  
 [10] J.S. Marchant and I. Parker, *EMBO J.* **20**, 65 (2001).  
 [11] L.S. Jouaville, F. Ichas, E.L. Holmuhamedov, P. Camacho, and J.D. Lechleiter, *Nature (London)* **377**, 438 (1995).  
 [12] J.D. Lechleiter, L.M. John, and P. Camacho, *Biophys. Chem.* **72**, 123 (1998).  
 [13] A.H. Cornell-Bell, S.M. Finkbeiner, M.S. Cooper, and S.J. Smith, *Science* **247**, 470 (1990).  
 [14] J.H. Horne and T. Meyer, *Science* **276**, 1690 (1997).  
 [15] A. Atri, J. Amundson, D. Clapham, and J. Sneyd, *Biophys. J.* **65**, 1727 (1993).  
 [16] R. Kupferman, P.P. Mitra, P.C. Hohenberg, and S.S.H. Wang, *Biophys. J.* **72**, 2430 (1997).  
 [17] A. McKenzie and J. Sneyd, *Int. J. Bifurcation Chaos Appl. Sci. Eng.* **8**, 2003 (1998).  
 [18] J. Keizer and G.D. Smith, *Biophys. Chem.* **72**, 87 (1998).  
 [19] J. Wagner, Y. Li, J. Pearson, and J. Keizer, *Biophys. J.* **75**, 2088 (1998).  
 [20] B.J. Roth, S.V. Yagodin, L. Holtzclaw and J.T. Russell, *Cell Calcium* **17**, 53 (1995).  
 [21] A.E. Bugrim, A.M. Zhabotinsky, and I.R. Epstein, *Biophys. J.* **73**, 2897 (1997).  
 [22] J. Keizer, G.D. Smith, S. Ponce-Dawson, and J.E. Pearson, *Biophys. J.* **75**, 595 (1998).  
 [23] S.P. Dawson, J. Keizer, and J.E. Pearson, *Proc. Natl. Acad. Sci. U.S.A.* **96**, 6060 (1999).  
 [24] M. Falcke, L.S. Tsimring, and H. Levine, *Phys. Rev. E* **62**, 2636 (2000).  
 [25] J.W. Shuai and P. Jung, *Proc. Natl. Acad. Sci. U.S.A.* **100**, 506 (2003).  
 [26] G.W. De Young and J. Keizer, *Proc. Natl. Acad. Sci. U.S.A.* **89**, 9895 (1992).  
 [27] J.W. Shuai and P. Jung, *Phys. Rev. Lett.* **88**, 68102 (2002).  
 [28] J.W. Shuai and P. Jung, *Biophys. J.* **83**, 87 (2002).  
 [29] Y. Li and J. Rinzel, *J. Theor. Biol.* **166**, 461 (1994).  
 [30] S.V. Yagodin, L. Holtzclaw, C.A. Sheppard, and J.T. Russell, *J. Neurobiol.* **25**, 265 (1994).  
 [31] E. Katayama, H. Funahashi, T. Michikawa, T. Shiraishi, T. Ikemoto, M. Iino, K. Hirose, and K. Mikoshiba, *EMBO J.* **15**, 4844 (1996).  
 [32] N.L. Albritton, T. Meyer, and L. Streyer, *Science* **258**, 1812 (1992).  
 [33] N. Callamaras, J.S. Marchant, X. Sun, and I. Parker, *J. Physiol. (London)* **509**, 81 (1998).